## Electron transfer drives the photosensitized polymerization of contrast agents

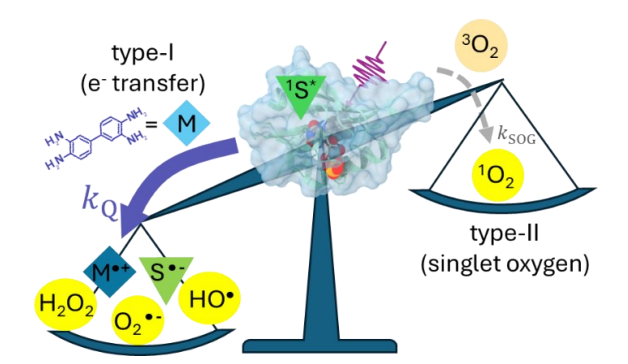
## by flavoprotein tags for correlative microscopy

- Mohd Sajid Lone<sup>1</sup>, Olga D. Merino-Chavez<sup>1,2</sup>, Nathan J. Ricks<sup>1,2</sup>, Ming C. Hammond<sup>1,2\*</sup>,
- 4 Rodrigo Noriega<sup>1\*</sup>
- <sup>1</sup> Department of Chemistry, University of Utah, Salt Lake City, UT 84112, USA
- 6 <sup>2</sup> Henry Eyring Center for Cell and Genome Science, University of Utah, Salt Lake City, UT 84112, USA
- \* Contact: ming.hammond@utah.edu, noriega@chem.utah.edu

#### 8 TOC graphic

1

2



# 10 ABSTRACT

9

11

12

13

14

15

16

17

18

19

20

21

Singlet oxygen generation has long been considered the key feature that allows genetically-encodable fluorescent tags to produce polymeric contrast agents for electron microscopy. Optimization of the singlet oxygen sensitization quantum yield has not included the effects of electron-rich monomers on the sensitizer's photocycle. We report that, at monomer concentrations employed for staining, quenching by electron transfer is the primary deactivation pathway for photoexcitations. A simple photochemical model including contributions from both processes reproduces the observed reaction rates and indicates that most of the product is driven by pathways that involve electron transfer with monomers – not by the sensitization of singlet oxygen. Realizing the importance of these competing reaction pathways offers a new paradigm to guide the development of genetically-encodable tags and suggests opportunities to expand the materials scope and growth conditions for polymeric contrast agents (e.g., biocompatible monomers, O<sub>2</sub>-poor environments).

#### INTRODUCTION

22

23

24

25

26

27

28

29

30

31

32

33

34

35

36

37

38

39

40

41

42

43

44

45

46

Genetically-encodable probes that can drive chemical transformations in a localized manner via optical means while also serving as efficient fluorescence emitters enable unique opportunities to advance highresolution biological imaging, sensing, and control.[1] Engineered flavoproteins are an important class of dual function tags because their flavin chromophores are known to have sizable fluorescence yield and the ability to sensitize singlet oxygen (1O2) species in solution.[2] These protein tags – and sensors based upon them – have been broadly applied in correlative light-electron microscopy (CLEM), where emitted photons are detected in fluorescence imaging while photogenerated reactive species support the oxidative polymerization of contrast agents for electron microscopy.[3-13] While the structure-function relationships dictating the photophysics behind the fluorescence and singlet oxygen generation (SOG) channels of engineered flavoproteins have been studied in detail, [14-19] the photochemical mechanism for downstream contrast agent growth has received considerably less attention. To date, the design of flavoproteins as dual-function CLEM tags has been predicated on their ability to photosensitize singlet oxygen, which is expected to drive the oxidation of electron-rich amine-containing aromatic monomers into melanoid polymers with effective metal-chelation properties.[5, 20, 21] This paradigm led to the design of miniSOG, a protein tag derived from the LOV2 domain of Arabidopsis thaliana phototropin 2.[3] Moreover, mutations to remove electron-rich amino acid residues surrounding miniSOG's flavin mononucleotide (FMN) cofactor led to protein variants with longer triplet lifetimes and significantly larger SOG yields; the flavoprotein with the largest reported SOG yield is SOPP3 ( $\eta_{SOC}^{SOPP3}$  = 0.60).[17] However, the current framework does not account for the possibility that the presence of monomers can alter the photophysical cycle of the sensitizer; thus, the photophysics of flavoproteins have been characterized and optimized in the absence of monomer. Yet, because the intended purpose of these dual-function protein tags is to photosensitize the oxidative polymerization of electron-rich monomers into metal-chelating melanoid polymers, the direct interaction of monomer species and photoexcited sensitizers should not be overlooked.

The oxidative coupling synthesis of melanoid polymers follows a complex reaction mechanism that yields heterogeneous products and is strongly dependent on solvent conditions. [22] Although it is possible to obtain melanoid polymers from a variety of amine-bearing monomers, [23-25] 3,3'-diaminobenzidine (DAB) has been the monomer of choice for CLEM contrast agents due to its established use in immunohistochemistry stains. [26, 27] Important limitations to the application of DAB in high-resolution imaging are its low membrane permeability, the lack of control on its diffusion and precipitation, and its toxicity. [26, 28] Biocompatible catecholamines and indolamines are viable DAB substitutes because they polymerize into similar melanoid materials [29]. In particular, dopamine (DA) is a favorable starting point for mechanistic studies of contrast agent growth due to the substantial body of work on its oxidation product, polydopamine.[23, 30-32] Polydopamine nanoparticles can be easily stained with heavy metals to achieve contrast in electron microscopy (Fig. S1). Herein, we identify the role of type-I photochemical pathways in oxidative polymerization reactions driven by dual-function flavoprotein tags by measuring their reaction rates as a function of sensitizer, illumination parameters, and solution conditions. To explore the role of intrinsic sensitizer photophysics, two widely-used flavoprotein tags (the original miniSOG variant and the SOG recordholder SOPP3, Scheme 1 and Fig. S2) were compared to unbound FMN and to flavin-adenosine dinucleotide (FAD). This choice for sensitizers was intended to achieve large variations in the environment of the flavin chromophore unit – as evidenced by their singlet and triplet excitation lifetimes, radiative and nonradiative decay rates, rate of intersystem crossing, and rate of oxygen sensitization, which have been extensively reported (Fig. S3, Table S1). To determine the effect of monomers on the photocycle of these sensitizers, we measured the bimolecular quenching rates of photoexcited sensitizers by the prototypical DAB monomer and the alternative DA. We found that, at monomer concentrations typically used for polymer growth, the primary deactivation pathway for photoexcitations is through electron transfer from monomers, which leads to type-I oxidation reactions. This observation prompted us to construct a simple photochemical model to describe the polymerization kinetics (Scheme 1). In this model, light absorption takes the sensitizer chromophore from the ground state (S<sub>0</sub>) to the singlet excited state (<sup>1</sup>S\*), which can return to the ground state by a

47

48

49

50

51

52

53

54

55

56

57

58

59

60

61

62

63

64

65

66

67

68

69

70

71

combination of radiative and nonradiative pathways or undergo intersystem crossing to the triplet excited state (3S\*). Decay of triplet excited states to the singlet ground state is a slow, spin-forbidden process, and this long-lived state can sensitize molecular oxygen (a triplet, <sup>3</sup>O<sub>2</sub>) via energy transfer and generate singlet oxygen (1O2), a well-established reactive oxygen species (ROS). This energy transfer mechanism to generate <sup>1</sup>O<sub>2</sub> is known as type-II photosensitization. When monomers (M) are present, they can quench photoexcited chromophores via electron transfer, yielding a sensitizer radical anion (S<sup>•-</sup>) whose electron transfer to oxygen yields superoxide ( $S^{\bullet-}+O_2 \rightarrow S_0 + O_2^{\bullet-}$ ) and leads to a cascade of reactions that generate a ROS including hydrogen peroxide (H<sub>2</sub>O<sub>2</sub>) and hydroxyl radicals (OH•). This electron transfer pathway to generate ROS is known as type-I photosensitization.[33] The initial photoinduced electron transfer step (M  $+S^* \rightarrow M^{\bullet +} + S^{\bullet -}$ , where S\* can be either singlet or triplet) also generates the radical cation of monomer  $(M^{\bullet+})$ , which acts as an additional reactive species whose oxidation and coupling leads to product formation. Our results indicate that type-I reactions which begin with electron transfer from monomers are a major player in the photosensitized growth of melanoid polymers by genetically-encodable flavoprotein tags – in contrast to the present framework centered on their ability to sensitize singlet oxygen. These results point to a richer design landscape for flavoproteins (and dual-function tags in general) that requires their consideration as a component of a larger photochemical system, placing a stronger emphasis on the properties of and interactions with reactive species previously regarded as decoupled from the evolution of photoexcitations.

73

74

75

76

77

78

79

80

81

82

83

84

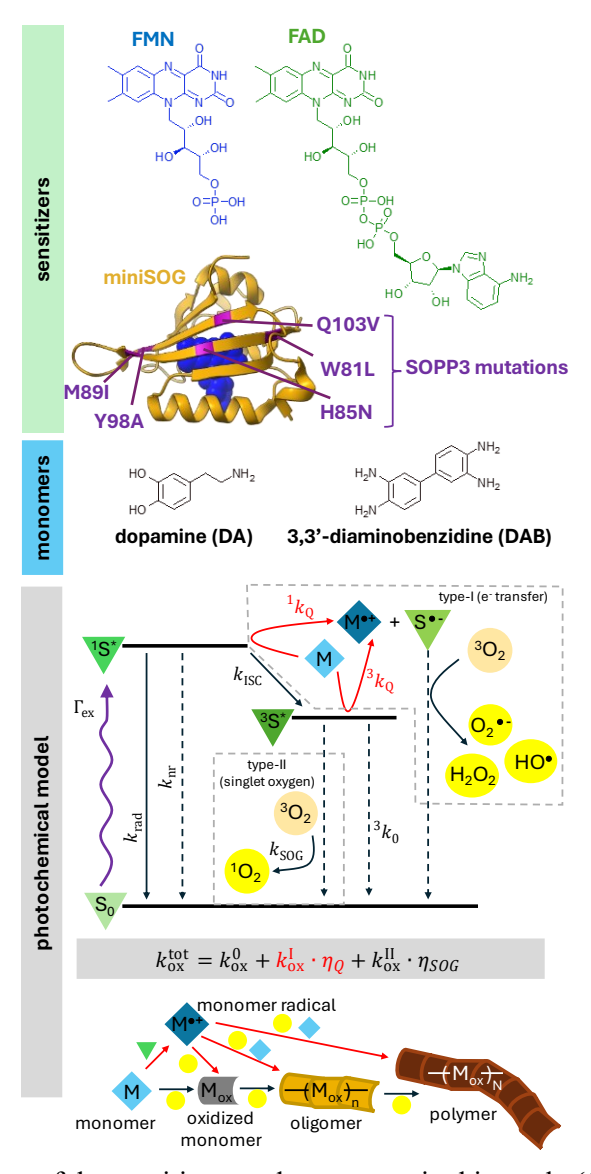
85

86

87

88

89



**Scheme 1.** Chemical structures of the sensitizers and monomers in this work. **(top)** Flavin mononucleotide (FMN) in blue, flavin adenosine dinucleotide (FAD) in green. Flavoprotein backbones are shown as ribbons, with miniSOG in gold and the mutations from miniSOG to SOPP3 shown in purple. In flavoproteins, the FMN cofactor shown as spheres in blue. **(middle)** The two monomers, dopamine (DA) and 3,3'-diaminobenzidine (DAB), contain amine groups and electron-rich aromatic rings whose oxidative coupling leads to melanoid polymers. **(bottom)** A Jablosnki diagram to illustrate the proposed photochemical model, with labels to identify the sensitizer (S), monomer (M), molecular oxygen, and reactive oxygen species. The rates for the evolution of excited states are shown, as well as their interaction with molecular oxygen and monomer species. Arrows in red denote the electron transfer events that lead to type-I reactions whose importance is highlighted in this work. The observed reaction rate is made up of a dark component  $(k_{ox}^0)$ , a combined rate from all type-I reactive species  $(k_{ox}^1)$  multiplied by the probability of electron transfer  $(\eta_Q)$ , and a rate from type-II pathway  $(k_{ox}^{II})$  multiplied by the probability of singlet oxygen generation  $(\eta_{SOG})$ . A simplified diagram of the reactions involved in oxidative polymerization is also shown.

We measured the rate of photopolymerization of DA and DAB by monitoring the time-dependent concentration of reaction products with kinetic absorbance experiments. Differential absorbance measurements as a function of reaction time contain information on the changing population of species in the path of the probe beam – conversion of reagent A into product B is associated with the loss of the reactant's transition moment  $(\vec{\mu}_A)$  and the gain of the product's transition moment  $(\vec{\mu}_B)$ , with an overall signal  $\Delta \vec{\mu} = \vec{\mu}_B - \vec{\mu}_A$ . Because our instrument employs a tungsten-halogen lamp with spectral output from the near ultraviolet to the near infrared (350-1000 nm), our data contains only the increased absorbance due to products (DA and DAB monomers absorb in the deep UV). The resulting kinetic spectra are well described by three Gaussian lineshapes (Fig. 1), two narrower features at shorter wavelengths and a considerably broader component at longer wavelengths. To interpret these kinetic spectra one must consider that the oxidative polymerization of DA and DAB is a multistage process involving several electron transfer, proton transfer, and intramolecular reorganization steps before reaching a polymer product with a flexible structure and large heterogeneity in monomer oxidation state and inter-monomer linkages. The redshifted absorption feature has been ascribed to this polymer product whose substantial structural disorder leads to considerable lineshape broadening (Fig. S4-S5), while the other features appear earlier and are consistent with oxidized monomer intermediates (narrow lineshape at higher photon energies) and oligomeric species (intermediate breadth and energy, closer to those of the polymer). As the reaction progresses, the amplitude for each of these Gaussian components increases, and the slope of the linear growth region is used to determine the reaction rates associated with each feature  $-k_{\text{Mox}}, k_{\text{oligo}}$ , and  $k_{\text{poly}}$ , respectively. The time lag in the appearance of polymer products is best interpreted by first considering each monomer's oxidation reaction. Dopamine oxidation to polydopamine involves several oxidation and cyclization steps to form semiquinone, quinone, and indole intermediates which undergo oxidative coupling into larger oligomeric and polymeric species.[34] In contrast to polydopamine's more complex reaction, DAB only requires a single electron transfer oxidation step to form the quinone iminium radical that can undergo oxidative coupling.[35] This more direct oxidative coupling pathway for DAB may also be

107

108

109

110

111

112

113

114

115

116

117

118

119

120

121

122

123

124

125

126

127

128

129

130

responsible for its effective polymerization, achieving similar yields to dopamine at lower concentrations. The concentration of monomers in these reaction mixtures was chosen to mimic experimental conditions in practical applications: [DAB]=0.32 mM is at the lower end of the amount used in staining procedures where [DAB]=0.3-5 mM,[3-5] while [DA]=25 mM is within the range used to generate polydopamine coatings, [DA]=10-55 mM.[36, 37] To balance the requirements for fluorescence imaging of biological samples followed by heavy metal staining for electron microscopy, this work was carried out in aqueous Tris buffer at pH 7 (details in SI).

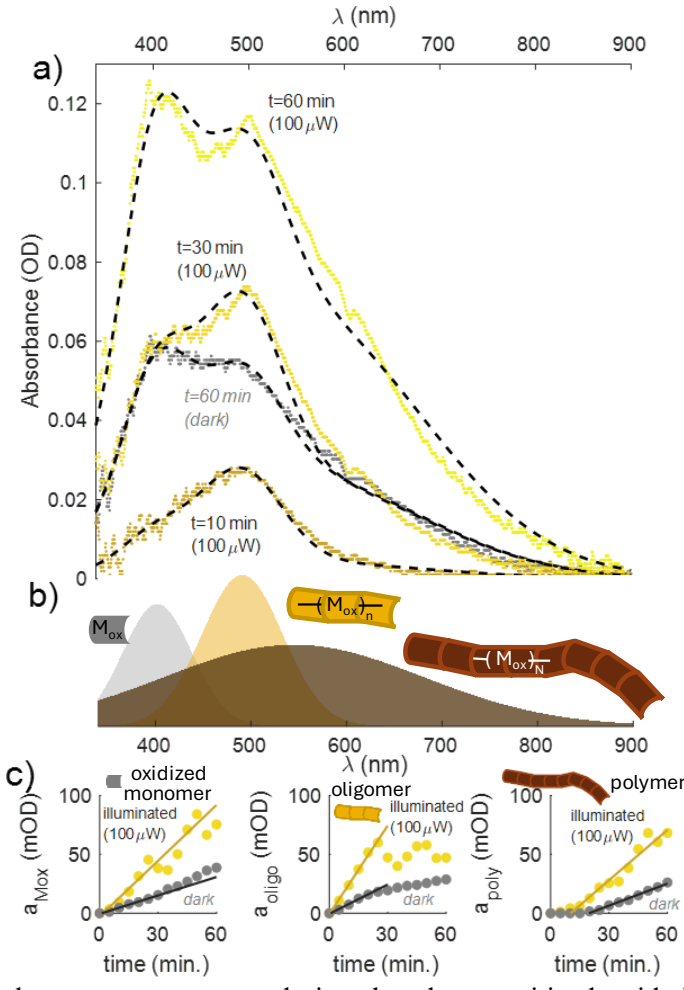


**Figure 1.** Kinetic absorbance measurements during the photosensitized oxidation of dopamine by the flavoprotein miniSOG ( $100 \, \mu W$  excitation power at a wavelength of  $475 \, \text{nm}$ ). A subset of the absorbance spectra shows their increasing amplitude over the  $60 \, \text{min}$  reaction (yellow curves); achieving a larger product conversion compared to an identical reaction in the absence of photoexcitation (gray curve). Each kinetic spectrum is described by a linear combination of three Gaussian features (**b**) corresponding to absorbance by oxidized monomer, oligomeric species, and polymer product. Fits to each of the spectra in (**a**) are shown as dashed lines. (**c**) The time-dependent amplitude for each absorption feature show the

increase in reaction rate from dark to light conditions (gray and yellow, corresponding to data from a), with linear fits used to obtain reaction rates shown as solid lines.

147

148

149

150

151

152

153

154

155

156

157

158

159

160

161

162

163

164

165

166

167

168

169

170

171

For each of the monomers used, the oxidative polymerization reaction rates depend on the excitation intensity, the choice of sensitizer, and solution conditions (e.g., pH, dissolved oxygen content). To ascertain the role of competing light-induced reaction pathways, we carried out experiments for each monomersensitizer pairing at various illumination intensities (with at least N=2 replicates per reaction condition) - average rates are reported in **Table 1**; traces for each Gaussian lineshape in **Fig. S6**. As expected, higher excitation intensities lead to faster reaction rates, protein-encased chromophores (miniSOG, SOPP3) are effective photosensitizers, and the slowest rates are observed for FAD. Importantly, photoexcitation only leads to polymer formation in the presence of sensitizer, ruling out direct excitation of monomers (Fig. S7). The ratio of dopamine M<sub>ox</sub>/oligomer amplitudes was observed to increase over time (Fig. S8) due to a plateau or decrease in oligomer absorbance that roughly coincides with the lag in polymer formation, which occurs earlier when the reaction rate is increased upon illumination - a possible indication that photogenerated species are more effective at driving polymerization than those generated in dark reactions. In oxygen-rich solutions, the photogenerated ROS responsible for monomer oxidation are likely hydroxyl radicals – especially given dopamine's propensity to oxidize in alkaline conditions. Oxidation by molecular oxygen has been proposed as an autooxidation pathway and is expected to contribute to dark reaction rates, which explains the reduction in dark reactions to negligible levels upon Ar bubbling (Fig. S9). However, product formation still occurs in low-O2 conditions when sensitizers are photoexcited, which indicates that monomer radicals' reactivity is not eliminated with the removal of dissolved molecular oxygen – although product formation proceeds with rates ~5-10X slower than equivalent photoexcited reactions in O<sub>2</sub>-rich solutions. This residual photoactivity in low-O<sub>2</sub> conditions is likely not the result of ROS, but instead due to photogenerated monomer radicals which may subsequently react with hydroxyl anions present in aqueous media or undergo photoaddition similar to that of psoralens.[38, 39] Future experiments using isotopically labeled (<sup>18</sup>O) water can help to determine the source of oxygen for this residual photoactivated

reactivity, and comparison to non-labeled solutions saturated with <sup>18</sup>O-labeled O<sub>2</sub> gas can provide information on the oxygen source for the remaining dark and photoinduced contributions.

**Table 1:** Rate constants extracted from kinetic absorbance spectra, calculated as the slope of time-dependent amplitudes for absorption features due to the production of oxidized monomer  $(k_{Mox})$ , oligomer  $(k_{oligo})$ , and polymer  $(k_{poly})$ . Data shown are the average and standard error of the mean.

Sensitizer	Excitation	xcitation k <sub>Mox</sub> (x10 <sup>-5</sup>		OD/min k <sub>oligo</sub> (x10 <sup>-5</sup>		kpoly (x10-	0 <sup>-5</sup> OD/min)	
	power (µW)	DA	DAB	DA	DAB	DA	DAB	
	Dark	28±9	1	66±4		53±7		
FAD	50	40±0.2	12±1	96±3	10±0.4	65±6	4±2	
	100	51±1	18±3	116±1	13±2	70±6	7±0.2	
	200	70±3	36±5	146±1	34±2	91±4	19±7	
FMN	50	68±0.2	74±0.7	142±4	56±2	95±6	27±4	
	100	90±2	85±0.3	177±5	87±4	104±4	55±2	
	200	123±5	134±11	232±7	130±3	124±2	94±4	
miniSOG	100	136±20	91±0.2	244±6	217±7	157±15	57±2	
	200	135±20	109±1	299±37	262±3	169±15	84±2	
SOPP3	100	171±3.0	106±17	183±24	119±24	119±3	24±9	
	200	184±10	113±20	204±3	181±14	159±6	48±0.7	

It is important to determine the rate at which photoexcitations decay *via* electron transfer from the readily oxidized monomer into the hole left in the flavin's HOMO by the photoexcited electron[40] – the initial charge transfer event which leads to the generation of reactive species in type-I pathways. This additional decay channel alters the sensitizer's fluorescence lifetime from its intrinsic value,  $\frac{1}{\Box}\tau_0$ , to a value that depends on the monomer concentration [Q] as

182 
$$\left(\frac{1}{\Box}\tau\right)^{-1} = \left(\frac{1}{\Box}\tau_0\right)^{-1} + \frac{1}{\Box}\kappa_Q [Q]$$
 (Eq. 1)

where the bimolecular quenching rate  $\frac{1}{\square}\kappa_Q$  depends on the coupling of initial and final states, and can be modeled with a Marcus electron transfer formalism. We extract the bimolecular quenching rate  $\frac{1}{\square}\kappa_Q$  for each monomer-sensitizer pair using a Stern-Volmer analysis of the sensitizer's fluorescence lifetime as a function of monomer concentration (**Fig. 2**, time-resolved data in **Fig. S10**). Interestingly, for a given monomer, singlet excitations of protein-encased flavins have bimolecular quenching rates ( $\frac{1}{\square}\kappa_Q$ ) on the order of those for protein-free flavins – a result that suggests electron transfer between chromophore and monomer is not strongly affected by the protein residues that separate them. Regardless of the sensitizer used, quenching of its singlet excited state by DAB ( $\frac{1}{\square}\kappa_{DAB} \sim 10^{10} \text{ M}^{-1}\text{s}^{-1}$ ) was considerably faster than by DA ( $\frac{1}{\square}\kappa_{DA} \sim 10^9 \text{ M}^{-1}\text{s}^{-1}$ ). For practical monomer concentrations, the rate of quenching  $\frac{1}{\square}\kappa_Q$ .

 $[Q] \sim 10^7 - 10^8 \text{ s}^{-1}$  is comparable to the intrinsic singlet decay rate  $\left(\frac{1}{12}\tau_0\right)^{-1}$ ; and thus a substantial fraction of photoexcitations decay *via* electron transfer and initiate type-I reactions even before reaching the longer-lived triplet state, where they are even more susceptible to quenching. In the flavoproteins samples tested here, the proportion of singlets that are quenched by DA are 11% in miniSOG and 22% in SOPP3 (for DAB, these values are 11% and 3% of singlets, respectively).

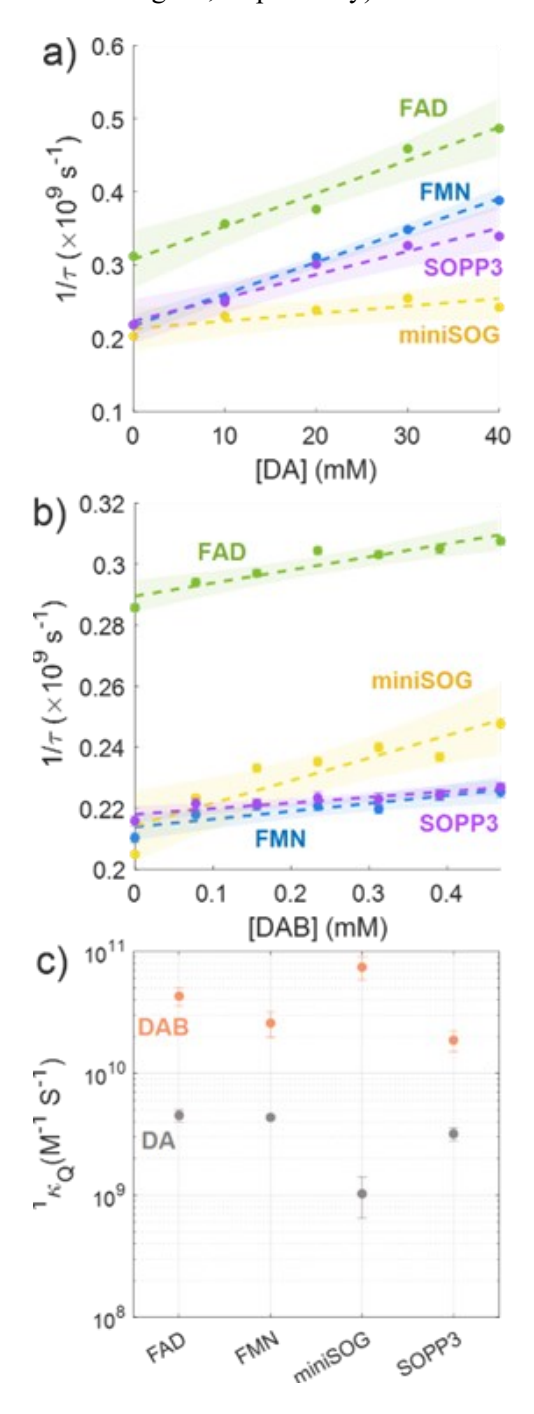


Figure 2: Stern-Volmer plots to quantify quenching rates for singlet photoexcitations by dopamine (a) and 3,3'-diaminobenzidine (b). Data collected for each sensitizer (markers) was fit to Eqn. 1 (dashed lines, 95% confidence intervals as shaded areas). Bimolecular quenching rate  ${}^{1}_{\square}\kappa_{Q}$  for each sensitizer-monomer pair shown in (c). Note the different scale in the x-axis for panels a and b, due to the different concentration range for DA and DAB. Separate plots for DAB quenching of FMN and SOPP3 are provided to better assess the quality of the fit (Fig. S11)

Electron transfer processes also take place from excited triplet states. However, triplet quenching rates are slower due to a reduction in the electronic coupling matrix element. Because our time-resolved fluorescence experiments probe dynamics in the <10 ns regime, triplet quenching rates were not accessible experimentally and are treated as proportional to singlet quenching rates with a ratio ( $\gamma = \frac{1}{12} \kappa_Q / \frac{3}{12} \kappa_Q$ ), which is greater than one. Comparison to an extensive data set of flavins quenched by amines,[40]  $\gamma$  spans four orders of magnitude – from 1.55 to  $1.57 \times 10^4$  – with most values in the  $2 \le \gamma \le 8$  window (the 10%-90% cutoffs for the cumulative distribution, **Fig. S12**). Given the much slower intrinsic decay rates for excited triplets (whose lifetimes are on the order of  $\mu$ s), electron transfer events are likely to play a significant role in triplet dynamics. In our analysis, we include  $\gamma$  as a fitting parameter in regression models (details below). This assumption is supported by comparison to a broad library of quenchers and validated by the model's relatively flat response in the range  $1 < \gamma < 300$  (**Figs. 3,4**) – a realistic range for these materials.

The importance of electron transfer is not limited to changes in the sensitizer photocycle; they result in reactive species and drive the growth of melanoid polymers. Thus, we include these additional pathways in a photochemical model (**Scheme 1**) to explain the variation in observed reaction rates (**Table 1**). This model must predict (1) the probability that a photoexcitation will result in a reactive species, and (2) the rate with which such reactive species yields a given product. The probability that state X will convert into state Y by a certain pathway is expressed as the rate of this process divided by the total rate leaving the initial state – e.g., the probability that a singlet excited state will lead to photon emission is the ratio of its radiative rate to the total rate of singlet decay,  $\frac{1}{\Box}k_{\rm rad}/\frac{1}{\Box}k_{\rm tot}$ . Our model to describe the time evolution of product formation adds all contributions from each pathway into a combined reaction rate which is modulated by

the yield of the initial branching step – the probability of sensitizing  ${}^{1}O_{2}$  times the rate at which it leads to products, vs. the probability of undergoing photoinduced electron transfer  $(M + S^{*} \rightarrow M^{\bullet +} + S^{\bullet -})$  times the rate at which the resulting reactive species yield products. In this way, we use experimentally-determined rates of population evolution in the excited state manifold to construct our model as follows. The predicted reaction rate is the sum of four components: a background rate due to oxidation in the dark,  $k_{ox}^{0}$ ; plus three light-induced processes:

- 1) two type-I pathways in which the sensitizer excited singlet or triplet states are quenched by a monomer and these radicals yield products with a rate  $k_{\text{ox}}^I$ , by a combination of mechanisms involving the generation of reactive oxygen species by the sensitizer radical[31, 41] and the direct polymerization of monomer radicals. The contribution from these channels is dependent on the probability that a photoexcitation is quenched by the monomer while in the singlet excited state  $(\frac{1}{2}k_{\text{Q}}/\frac{1}{2}k_{\text{tot}})$  or after converting to a triplet state  $(k_{\text{ISC}}/\frac{1}{2}k_{\text{tot}} \times \frac{3}{2}k_{\text{Q}}/\frac{3}{2}k_{\text{tot}})$ ;
- a singlet-oxygen mediated (type-II) mechanism whose amplitude depends on the probability of intersystem crossing  $(k_{\rm ISC}/\frac{1}{\square}k_{\rm tot})$  times the likelihood that the triplet state sensitizes  $^{\rm I}{\rm O}_2$   $(k_{\rm SOG}/\frac{3}{\square}k_{\rm tot})$ , and the rate with which  $^{\rm I}{\rm O}_2$  converts reactants into products  $(k_{\rm ox}^{II}=\alpha\cdot k_{\rm ox}^I)$ , where the relative efficiency of product yield by type-I and type-II processes is explicitly included in the proportionality factor  $\alpha$ ).

Adding each contribution to the overall reaction rate, we obtain Eq. 2, where the three terms inside the square brackets represent the contributions from each of the light-induced components – respectively, type-I events from the singlet and triplet state, and singlet oxygen mediated type-II process. For simplicity, the rate of oxidation and the illumination flux are grouped into a power-dependent prefactor ( $\Gamma_{ex}k_{ox}^{I}=P_{ex}\kappa_{pre}$ ).

$$k_{model} = k_{ox}^{0} + P_{ex} \kappa_{pre} \times \left[ \left( \frac{\frac{1}{\Box} k_{Q}}{\frac{1}{\Box} k_{tot}} \right) + \left( \frac{k_{ISC}}{\frac{1}{\Box} k_{tot}} \cdot \frac{\frac{1}{\Box} k_{Q} / \gamma}{\frac{3}{\Box} k_{tot}} \right) + \alpha \cdot \left( \frac{k_{ISC}}{\frac{1}{\Box} k_{tot}} \cdot \frac{k_{SOG}}{\frac{3}{\Box} k_{tot}} \right) \right]$$
 (Eq. 2)

In this way, the total reaction rate is determined entirely by a constant dark reaction, the illuminationdependent population flux into the photoexcited sensitizer, the evolution of the sensitizer's excited state

into productive and non-productive species, and the reaction rate for these reactive species. The only fitting parameters in Eqn. 2 are the rate prefactors  $\kappa_{pre}$  (one for each species monitored;  $\kappa_{pre}^{Mox}$ ,  $\kappa_{pre}^{oligo}$ , and  $\kappa_{pre}^{poly}$ ), the relative efficiency of type-I and type-II sensitized oxidation ( $\alpha$ ), and the ratio of singlet and triplet quenching rates  $(\gamma)$ . All remaining inputs for this model are independent variables such as experimental conditions (illumination power  $P_{ex}$ , monomer concentration [Q]), or observables measured in this study or reported in the literature (intrinsic values for the lifetime of singlets,  $\tau_0$ , and triplets,  $\tau_0$ ; quantum yields for fluorescence,  $\eta_{fl}^0$ , intersystem crossing,  $\eta_{\Delta}^0$ , and singlet oxygen generation  $\eta_{SOG}^0$ ; as well as the bimolecular singlet quenching rate  $^1_{\square}\kappa_{\mathrm{Q}}$  and the dark reaction rates for each species  $k^{\,0}_{\,\mathrm{Mox}},\,k^{\,0}_{\,\mathrm{oligo}},$  and  $k_{\text{poly}}^{0}$ ), which are collected in Table S1. Explicitly writing the kinetics governing excited state evolution in each stage of the photocycle, it is possible to express Eq. 2 as a function of these observable quantities (see Eqs. S1-S6 and details therein). Using least-squares regression, Eq. 2 was fitted to each set of experimentally observed reaction rates – data from DA and DAB were treated separately because the reaction prefactors, the relative efficiency of type-I and type-II sensitized oxidation ( $\alpha$ ), and the ratio of singlet and triplet quenching rates ( $\gamma$ ) are expected to depend on the monomer undergoing oxidative polymerization. For both monomers in this study, the rate predicted by Eqn. 2 shows remarkable agreement with the observed trends in reaction rates for melanoid polymers and monomer oxidation intermediates (Fig. 3), with values spanning more than an order of magnitude in rate. Both regression models reveal reaction prefactors in the range  $5-20~\mathrm{OD^{-1}\cdot min^{-1}}$  $W^{-1}$  and following the trend  $\kappa_{pre}^{oligo} > \kappa_{pre}^{Mox} > \kappa_{pre}^{poly}$ ; however, we must note that these values represent the absorbance of each species, which is the product of its concentration and molar extinction coefficient. Although monomer concentration is considerably larger (~100X) for DA vs. DAB, their reaction prefactors are comparable – a consequence of using reaction conditions similar to those optimized in applications where high product yield was the desired outcome (i.e., staining, coating). While best-fit parameters for

250

251

252

253

254

255

256

257

258

259

260

261

262

263

264

265

266

267

268

269

270

271

272

273

274

reaction prefactors are well-defined, the regression results have a significantly reduced sensitivity to the

parameters for reaction efficiency and quenching rate ratio ( $\alpha$  and  $\gamma$ ), as evidenced by their large confidence

intervals. Nevertheless, these best-fit values for  $\gamma$  are in the range expected for electron-rich aromatic amine quenchers (**Fig. S12**), and the result of  $\alpha \sim 0$  indicates the substantial importance of type-I processes in these reactions.

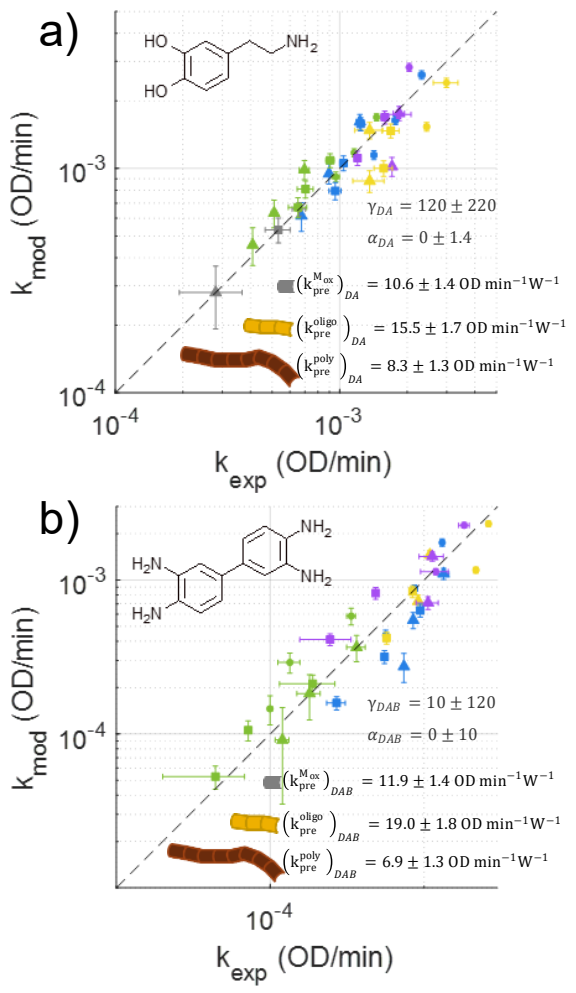


Figure 3: Model outcomes for the photosensitized oxidative polymerization of dopamine (a) and 3,3'-diaminobenzidine (b). Measured vs. predicted reaction rates for oxidized monomer (▲), oligomer (●), and polymer (■) for all sensitizers (FMN=blue, FAD=green, miniSOG=yellow, and SOPP3=purple) as well as in the dark (gray). Dashed line indicates 1:1 correspondence between experimental observations (x-axis) and model prediction (y-axis). Model parameters obtained from least-squares regression are shown in each panel (along with their standard error).

To explore the behavior of this model and extract further insight, we performed a series of regressions where the type-I vs. type-II reaction efficiency ( $\alpha$ ) and singlet vs. triplet quenching rate ratio ( $\gamma$ ) were varied over the range  $0 < \alpha < 3$  and  $1 < \gamma < 10^3$ , keeping these parameters constant using the reaction prefactors as fitting variables. The broad region of  $\alpha$  and  $\gamma$  values for which the residuals are close to their minimum

(Fig. 4a-b) sheds light on the reduced sensitivity to these variables displayed by the regression models in Fig. 3. For dopamine polymerization reactions, let us consider the region where the residuals (represented by the summed squared error, SSE) deviate by up to 1% from their minimum. For this subset of models, the average values for  $\langle \alpha_{DA} \rangle_{1\%} = 0.05 \pm 0.01$  and  $\langle \gamma_{DA} \rangle_{1\%} = 39 \pm 2$ , as well as the fitted reaction prefactors (Fig. 4c-d) follow the trends and values determined by the earlier results (Fig. 3a). Furthermore, it is possible to calculate the fraction of the photoinduced reaction rate due to type-I vs. type-II pathways for each of the sensitizers (Fig. 4e-f). For all models with residuals within 1% of their minimum, over 98% of the photoinduced reaction rate can be explained by type-I pathways. For 3,3'-diaminobenzidine polymerization reactions, models within the 1% boundary for deviation from the SSE minimum report average values  $\langle \alpha_{DAB} \rangle_{1\%} = 0.26 \pm 0.02$  and  $\langle \gamma_{DAB} \rangle_{1\%} = 14 \pm 1$  and reaction prefactors in agreement with results from the initial regression (Fig. 3b). Although lower than that for DA reactions, the fraction of the photoinduced reaction rate due to type-I processes is still substantial – particularly for flavoprotein sensitizers: for models with residuals within 1% of their minimum, the photoinduced rate due to type-I pathways is >63% for FMN, >75% for FAD, >99% for miniSOG, and >98% for SOPP3.

The importance of type-I pathways is better understood by considering the competition between the singlet oxygen generation rate and the triplet quenching rate. In the absence of monomer, the SOG rate  $k_{SOG} \sim 10^3 - 10^4 \text{ s}^{-1}$  is comparable to the triplet decay rate  $\left(\frac{3}{10}\tau_0\right)^{-1}$  – thus the sizable intrinsic SOG yields in these sensitizers. However, in the presence of electron-rich aromatic amines like DA and DAB, electron transfer triplet quenching is a more effective pathway because quenching rates at the monomer concentrations used in applications,  $\frac{3}{10}k_Q = \left(\frac{1}{100}k_Q \cdot [Q]\right)/\gamma \sim 10^5 - 10^6 \text{ s}^{-1}$ , are considerably larger than the singlet oxygen generation rate. In order to allow photoexcited flavoproteins to efficiently sensitize singlet oxygen, the concentration of monomers in solution would need to be lowered by a factor of 20-60X. However, this strategy to control the reaction mechanism has the downside of slowing the reaction rate in two ways: lowering the concentration of polymer building blocks and reducing the rate of generation for reactive species – with a concomitant increase in the staining time.

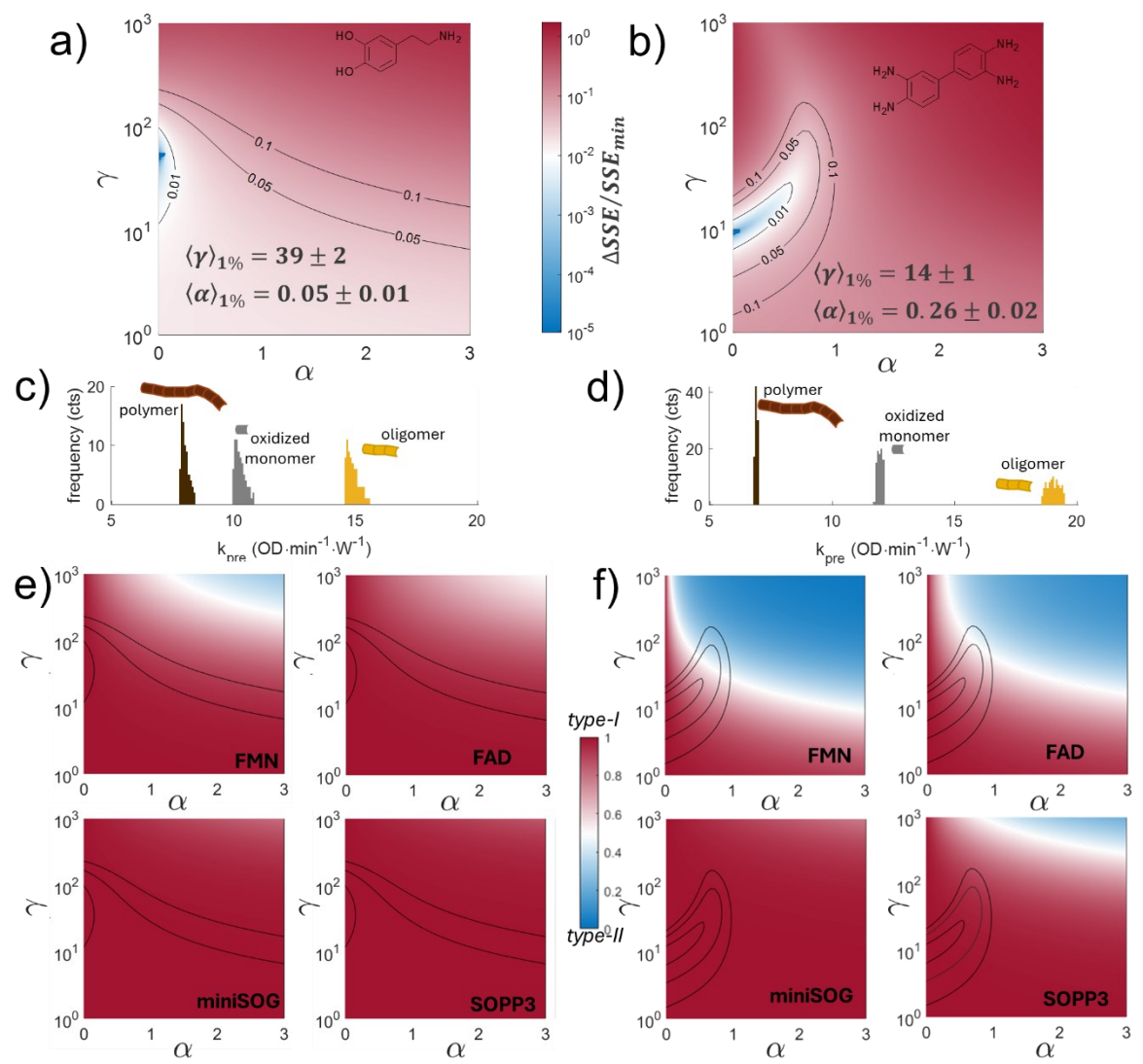


Figure 4: Regression models for fixed values of type-I vs. type-II reaction efficiency ( $\alpha$ ) and singlet vs. triplet quenching rate ratio ( $\gamma$ ). The sum of squared errors (SSE) for models of dopamine (a) and 3,3'-diaminobenzidine (b) polymerization show a shallow minimum, as expected due to the reduced sensitivity to these parameters displayed by models in Fig. 3. Regressions in (a,b) combine observations from all sensitizers (sensitizer-specific effects of  $\alpha$  and  $\gamma$  shown in panels e-f). Colormap in panels (a,b) denotes the relative change in SSE from their minimum; contour lines demarcate regions where SSE is within 1%, 5%, and 10% of the minimum. For models with SSE within 1% of the minimum, the reaction rate prefactors for each species are clustered around well-defined values (c,d) in agreement with results in Fig. 3. In panels (e,f), the fraction of the photoinduced reaction rate due to type-I vs type-II pathways is shown for each sensitizer, indicating the predominant contribution of a type-I mechanism. Contour lines for SSE values taken from (a,b) are overlaid in (e,f) to assist in evaluating the goodness of fit across models.

In summary, accounting for the contributions of competing reaction pathways in polymer contrast agent growth is a key step to optimize their properties. When designing dual-function genetically-encodable tags, it is not only necessary to enhance the SOG efficiency in pristine buffer conditions, we must consider the competition between type-II singlet oxygen generation and electron transfer quenching of photoexcited states leading to type-I reactions. For typical monomer concentrations, electron transfer quenching is a dominant decay pathway. Indeed, we found that the photosensitized oxidative polymerization of dopamine and 3,3'-diaminobenzidine into metal-chelating melanoid materials is strongly driven by type-I mechanism. These results stand in contrast to the widespread assumption that singlet oxygen generation is the central characteristic to be optimized when designing dual-function genetically encodable tags for correlative microscopy.[42, 43] However, because charge transfer events between monomers and photoexcited sensitizers lead to radical species (M\*\*, S\*\*) that support productive polymerization pathways, leveraging these previously-neglected mechanisms can be an avenue to extend the applicability of dual-function genetically encodable tags. Some exciting implications of these results include the possibility to grow contrast agents in oxygen-poor conditions (such as in biofilms), broadening the monomer palette to other biocompatible monomers, and expanding the chemical diversity of sensitizers to systems previously ruled out by their low SOG efficiencies.

#### **ACKNOWLEDGMENTS**

This work was partially funded by the Immunology, Inflammation, and Infectious Disease (3i) Initiative at University of Utah Health (Team Development grant), ONR grant (N00014-21-1-2188) and NIH grant R01GM124589 to MCH, and NSF grant (MCB-2123516) to RN. OMC's contributions through the University of Utah Chemistry REU program were supported by the National Science Foundation (award 2150526). This work made use of University of Utah shared facilities of the Micron Technology Foundation Inc. Microscopy Suite sponsored by the John and Marcia Price College of Engineering, Health Sciences Center, Office of the Vice President for Research.

### **SUPPORTING INFORMATION**

Supporting information available online contains details regarding materials (including protein expression and purification); characterization of polymer nanoparticles and sensitizer photophysics; instrumentation,

- data, and analysis for kinetic absorbance experiments; comparisons of illuminated, dark, and Ar-bubbled
- 356 reactions; analysis of time-resolved photoluminescence quenching experiments; and construction of the
- 357 photochemical model.

359

#### **REFERENCES**

- 360 1. Beatty, K.E. and C.S. Lopez, *Characteristics of genetic tags for correlative light and electron microscopy.* Curr Opin Chem Biol, 2023. **76**: p. 102369.
- Zheng, F., et al., *Genetically encoded photocatalytic protein labeling enables spatially-resolved profiling of intracellular proteome.* Nature Communications, 2023. **14**(1): p. 2978.
- 3. Shu, X., et al., A Genetically Encoded Tag for Correlated Light and Electron Microscopy of Intact Cells, Tissues, and Organisms. PLOS Biology, 2011. **9**(4): p. e1001041.
- Boassa, D., et al., Split-miniSOG for Spatially Detecting Intracellular Protein-Protein Interactions
   by Correlated Light and Electron Microscopy. Cell Chemical Biology, 2019. 26(10): p. 1407 1416.e5.
- 369 5. Rodríguez-Pulido, A., et al., *Assessing the potential of photosensitizing flavoproteins as tags for correlative microscopy.* Chemical Communications, 2016. **52**(54): p. 8405-8408.
- 371 6. Boassa, D., et al., Mapping the subcellular distribution of  $\alpha$ -synuclein in neurons using genetically and encoded probes for correlated light and electron microscopy: implications for Parkinson's disease pathogenesis. J Neurosci, 2013. **33**(6): p. 2605-15.
- Boassa, D., et al., Pannexin2 oligomers localize in the membranes of endosomal vesicles in
   mammalian cells while Pannexin1 channels traffic to the plasma membrane. Frontiers in Cellular
   Neuroscience, 2015. 8.
- 8. Burgers, P.P., et al., *A small novel A-kinase anchoring protein (AKAP) that localizes specifically protein kinase A-regulatory subunit I (PKA-RI) to the plasma membrane*. J Biol Chem, 2012.

  287(52): p. 43789-97.
- 380 9. Cleyrat, C., et al., *Mpl Traffics to the Cell Surface Through Conventional and Unconventional Routes.* Traffic, 2014. **15**(9): p. 961-982.
- 382 10. Deerinck, T.J., et al., Fluorescence photooxidation with eosin: a method for high resolution 383 immunolocalization and in situ hybridization detection for light and electron microscopy. J Cell 384 Biol, 1994. **126**(4): p. 901-10.
- Ludwig, A., et al., Molecular Composition and Ultrastructure of the Caveolar Coat Complex. Plos
   Biology, 2013. 11(8).
- 387 12. Ou, H.D., et al., *Visualizing viral protein structures in cells using genetic probes for correlated light and electron microscopy.* Methods, 2015. **90**: p. 39-48.
- 389 13. Strickfaden, H., Z.Z. Xu, and M.J. Hendzel, Visualization of miniSOG Tagged DNA Repair Proteins
   390 in Combination with Electron Spectroscopic Imaging (ESI). Jove-Journal of Visualized
   391 Experiments, 2015(103).
- 392 14. Nikolaev, A., et al., *Fine spectral tuning of a flavin-binding fluorescent protein for multicolor imaging.* J Biol Chem, 2023. **299**(3): p. 102977.
- Souslova, E.A., K.E. Mironova, and S.M. Deyev, Applications of genetically encoded
   photosensitizer miniSOG: from correlative light electron microscopy to immunophotosensitizing.
   Journal of Biophotonics, 2017. 10(3): p. 338-352.

- Torra, J., et al., *Tailing miniSOG: structural bases of the complex photophysics of a flavin-binding singlet oxygen photosensitizing protein.* Scientific Reports, 2019. **9**.
- Westberg, M., et al., No Photon Wasted: An Efficient and Selective Singlet Oxygen
   Photosensitizing Protein. The Journal of Physical Chemistry B, 2017. 121(40): p. 9366-9371.
- Westberg, M., et al., *Temperature Sensitive Singlet Oxygen Photosensitization by LOV-Derived Fluorescent Flavoproteins.* The Journal of Physical Chemistry B, 2017. **121**(12): p. 2561-2574.
- 403 19. Ruiz-González, R., et al., *Singlet Oxygen Generation by the Genetically Encoded Tag miniSOG.*404 Journal of the American Chemical Society, 2013. **135**(26): p. 9564-9567.
- 405 20. Meisslitzer-Ruppitsch, C., et al., *Photooxidation technology for correlated light and electron microscopy.* J Microsc, 2009. **235**(3): p. 322-35.
- 407 21. Maranto, A.R., *Neuronal Mapping: A Photooxidation Reaction Makes Lucifer Yellow Useful for Electron Microscopy.* Science, 1982. **217**(4563): p. 953-955.
- 409 22. Hong, S., et al., *Non-Covalent Self-Assembly and Covalent Polymerization Co-Contribute to Polydopamine Formation.* Advanced Functional Materials, 2012. **22**(22): p. 4711-4717.
- 411 23. Lee, H., et al., *Mussel-inspired surface chemistry for multifunctional coatings.* Science, 2007. 412 **318**(5849): p. 426-430.
- 413 24. Nakatsuka, N., et al., *Polyserotonin Nanoparticles as Multifunctional Materials for Biomedical Applications*. Acs Nano, 2018. **12**(5): p. 4761-4774.
- Vogliardi, S., et al., *An investigation on the role of 5-hydroxytryptophan in the biosynthesis of melanins*. Journal of Mass Spectrometry, 2002. **37**(12): p. 1292-1296.
- 417 26. Beatty, K.E. and C.S. López, *Characteristics of genetic tags for correlative light and electron microscopy.* Current Opinion in Chemical Biology, 2023. **76**: p. 102369.
- 419 27. Ngo, J.T., et al., *Click-EM for imaging metabolically tagged nonprotein biomolecules.* Nat Chem 420 Biol, 2016. **12**(6): p. 459-65.
- 421 28. Adams, S.R., et al., *Multicolor electron microscopy for simultaneous visualization of multiple*422 *molecular species.* Cell chemical biology, 2016. **23**(11): p. 1417-1427.
- Lemaster, J.E., et al., Gadolinium Doping Enhances the Photoacoustic Signal of Synthetic Melanin
   Nanoparticles: A Dual Modality Contrast Agent for Stem Cell Imaging. Chemistry of Materials,
   2019. 31(1): p. 251-259.
- 426 30. Lv, Q., et al., *Photoacoustic Imaging Endometriosis Lesions with Nanoparticulate Polydopamine* 427 as a Contrast Agent. Advanced Healthcare Materials, 2023. **n/a**(n/a): p. 2302175.
- 428 31. Salomäki, M., et al., *Effects of pH and Oxidants on the First Steps of Polydopamine Formation: A*429 *Thermodynamic Approach.* The Journal of Physical Chemistry B, 2018. **122**(24): p. 6314-6327.
- 430 32. Mavridi-Printezi, A., et al., *Reversible Supramolecular Noncovalent Self-Assembly Determines the*431 *Optical Properties and the Formation of Melanin-like Nanoparticles.* The Journal of Physical
  432 Chemistry Letters, 2022. **13**(42): p. 9829-9833.
- 433 33. Baptista, M.S., et al., *Type I and Type II Photosensitized Oxidation Reactions: Guidelines and Mechanistic Pathways.* Photochem Photobiol, 2017. **93**(4): p. 912-919.
- 435 34. Hosoda, R., et al., *In situ infrared spectroscopy of dopamine oxidation/reduction reactions on a polycrystalline boron-doped diamond electrode.* Carbon, 2021. **171**: p. 814-818.
- 437 35. Nateghi, M.R., M.H. Mosslemin, and H. Hadjimohammadi, *Electrochemical preparation and characterization of poly (3,3'-diaminobenzidine): A functionalized polymer*. Reactive and Functional Polymers, 2005. **64**(2): p. 103-109.
- Kaya, K., S. Jockusch, and Y. Yagci, Mussel-Inspired Coatings by Photoinduced Electron-Transfer
   Reactions: Photopolymerization of Dopamine under UV, Visible, and Daylight under Oxygen-Free
   Conditions. Macromolecules, 2021. 54(13): p. 5991-5999.

- Tokura, Y., et al., Fabrication of Defined Polydopamine Nanostructures by DNA Origami-Templated Polymerization. Angewandte Chemie-International Edition, 2018. **57**(6): p. 1587-1591.
- 446 38. Hearst, J.E., *Psoralen photochemistry*. Annu Rev Biophys Bioeng, 1981. **10**: p. 69-86.
- 39. Schmitt, I.M., S. Chimenti, and F.P. Gasparro, *Psoralen-protein photochemistry--a forgotten field.* J Photochem Photobiol B, 1995. 27(2): p. 101-7.
- 40. Porcal, G., et al., *Electron transfer quenching of singlet and triplet excited states of flavins and lumichrome by aromatic and aliphatic electron donors.* Physical Chemistry Chemical Physics, 2003. **5**(19): p. 4123-4128.
- 452 41. Massad, W.A., et al., *Vitamin B2-sensitized Photo-oxidation of Dopamine*. Photochemistry and Photobiology, 2008. **84**(5): p. 1201-1208.
- Wang, J., et al., *Visible-light initiated polymerization of dopamine in a neutral environment for surface coating and visual protein detection.* Polymer Chemistry, 2018. **9**(42): p. 5242-5247.
- 43. Alfieri, M.L., et al., *Polydopamine at biological interfaces*. Advances in Colloid and Interface Science, 2022. **305**: p. 102689.